Received: 8 April 2020 | Revised: 18 June 2020 | Accepted: 10 September 2020

IET Image Processing

DOI: 10.1049/ipr2.12106

The Institution of Engineering and Technology WILEY

ORIGINAL RESEARCH PAPER

Segmentation of osteosarcoma in MRI images by K-means clustering, Chan-Vese segmentation, and iterative Gaussian filtering

Mohamed Nasor | **Walid Obaid**

Department of Biomedical Engineering, Ajman University, Ajman, UAE

Correspondence
Mohamed Nasor, Department of Biomedical Engineering, Ajman University, Ajman, UAE.
Email: m.nasor@ajman.ac.ae

Abstract

Unlike other types of tumours, automated osteosarcoma segmentation in magnetic resonance images (MRI) is a challenging task due to its different and unique intensity and texture. This paper presents a technique for segmenting osteosarcoma in MRI images using a combination of image processing techniques which include K-means clustering, Chan-Vese segmentation, iterative Gaussian filtering, and Canny edge detection. In addition, the proposed technique involves iterative morphological operations and object counting. The technique was tested using 50 MRI scan images that contain osteosarcoma tumours. The proposed technique was able to segment the osteosarcoma regardless of the variations in their intensities, textures and locations. The performance of the technique was measured by calculating the values for precision, recall, specificity, Dice score coefficient, accuracy and the running time (RT) for all tested cases. The proposed technique achieved 95.96% precision, 86.15% recall, 99.51% specificity, 89.84% Dice score coefficient, 98.02% accuracy, and 191.62 s average running time. This technique can assist clinicians in making treatment plans for patients with osteosarcoma.

1 | INTRODUCTION

Osteosarcoma which is also called osteogenic sarcoma is a malignant tumour in the skeletal bones. It is characterized by the formation of osteoid tissues or immature bone by the tumour cells. It affects the end of long bones such as the knee. It has three subtypes which include high-grade, medium-grade, and low-grade. People under the age of 25 (children and teenagers) are more prone to this tumour [1, 2].

In order to determine the rate of tumour tissue necrosis, histopathological analysis is performed which is laborious, time consuming and its accuracy depends on the expertise and judgment of the clinician. Moreover, response monitoring cannot be done during chemotherapy since it requires a resected tumour [3]. To solve these problems, non-invasive techniques such as MRI imaging are used for Osteosarcoma quantitative analysis in order to perform surgical procedures planning and treatment response monitoring. Automated segmentation techniques are generally faster and give accurate tumour quantification for preoperative planning of chemoradiation and postoperative therapeutic efficacy assessment in clinics [4].

There are various challenges that face automatic osteosarcoma tumour segmentation. One of these challenges is the variations in size, pixels' intensity, shape, and position of osteosarcoma tumours. Moreover, Osteosarcoma is not strictly restricted to bones, it can appear on adjacent soft tissues as well. [5]. Other challenges include the variations of pixel textures within the tumour itself and the close similarity between the tumourous tissues and normal surrounding tissues.

2 | PREVIOUS WORK

There are various medical image segmentation techniques - presented before in literature. Zhang et al., proposed a segmentation technique that involves hybrid clustering and morphological operations [6]. Another technique was proposed by Karuna

et al., for MRI segmentation using principal component analysis (PCA) and hybrid clustering algorithms [7]. A segmentation technique was proposed by Hu et al., for MRI images [8]. The technique used Gaussian-mixture model and region restricted dynamic programming. A segmentation technique proposed by Alsmadi used hybrid artificial bee colony (ABC) algorithm and fuzzy C-means algorithm [9].

Various techniques were proposed for segmenting osteosarcoma in medical images in particular. Frangi et al., Glass et al., and Chen et al. proposed learning-based techniques using a large number of selected features in order to achieve higher accuracy image segmenation [10–12]. An advanced learning-based method for reducing the number of features at the cost of accuracy was used by Tripathy et al., and Zhang et al. [13, 14]. Girshick et al., Kraus et al., Moeskops et al., and Zhang et al., Ertas et al., Pereira et al., and Long et al., proposed learning-based methods that use convolutional neural networks (CNN) (FCN) [15–21]. However, these methods were not effective in identifying small object regions. A cluster-based method proposed by Chen et al. which utilizes seed points for expansion. This technique has a relatively low performance due to the lack of prior knowledge of objects [22]. A bone tumour segmentation in MRI images was proposed by Frangi et al., using neural networks based approach [10]. The method comprises two-stage cascaded classifiers. The first stage differentiates between healthy and tumourous tissues while the second stage differentiates between viable and non-viable tumours. An Osteosarcoma segmentation algorithm was proposed by Ma et al., using vectorial fuzzy-connectedness segmentation [23]. An osteosarcoma segmentation technique was presented by Hong et al., based on the analysis of blood-perfusion exocrine pancreatic insufficiency (EPI) series using similarity mapping method and watershed with specific preprocessing to perform the segmentation [24]. A segmentation method was presented by Rajeswari et al., using spatial multiple criteria fuzzy clustering [25]. Another method was proposed by Mandava et al., for segmentation of osteosarcoma in MRI images using dynamic harmony and Fuzzy C-means clustering [26]. An automatic recognition method of lesion areas in osteosarcoma X-ray images was proposed by Li and Liu [27]. The method was based on support vector machine using color and texture feature vectors. The authors reported 73% ± 11% accuracy. A fully automated approach for osteosarcoma segmentation in MRI images was proposed by Huang et al. [28]. The authors developed a conditional random field (CRF) model to incorporate multiple features. A method was presented by Zhang et al., based on multiple supervised residual network (MSRN) for osteosarcoma segmentation in CT images [29].

In this paper, we present an automatic technique for segmenting osteosarcoma in MRI images. The technique involves K-means clustering, Chan-Vese segmentation, iterative Gaussian filtering, iterative morphological operations, canny edge detection, region growing, and elimination of false regions. The main difference between this technique and previous osteosarcoma MRI segmentations is that the proposed technique can successfully segment the osteosarcoma in different MRI scan types such as T1-weighted, PD, and T2-weighted with different views: coronal (front to back) plane and sagittal (side-to-side) plane.

3 | METHODOLOGY

The proposed technique is comprised of K-means clustering, finding the largest surrounding edge, Chan-Vese segmentation, iterative Gaussian filtering, Canny edge detection, and region growing. The technique also includes morphological operations such as thinning, branch points elimination, and majority transformation. Figure 1 shows the block diagram of the proposed technique while Figure 2 shows MRI images of normal bones that represent the ground truth for comparison with bones with osteosarcoma [30–32].

The first step after obtaining the MRI image is performing K-means clustering. K-means is a well-known algorithm for clustering images into k regions by grouping pixels according to the similarity or dissimilarity of their feature vectors: $X = [x_i | i = 1, 2, 3, ...]$ around clusters centroids $C = [c_j | j = 1, 2, 3, ... k]$ [33]. The feature vectors of the k regions are obtained using Euclidean distances calculated by:

$$d = ||x_i - c_j||. \tag{1}$$

K-means is used to process the MRI image into four clusters: high-intensity cluster, medium-high intensity cluster, medium-low intensity cluster, and low-intensity cluster. The low-intensity cluster is discarded since it is very unlikely that it contains a tumour. The image then undergoes masking by the largest surrounding edge to remove false objects around the region of interest. The largest surrounding edge is obtained by multiplying the MRI image with a constant (n) and converting the image to binary using a large threshold value and performing morphological closing using a disk shape pattern with radius (r) coupled with filling of holes [34–36]. This process is repeated while increasing the constant (n) and the disk radius (r) gradually until the total number of detected objects becomes one. The extracted largest surrounding edge is shown in Figure 3. The next step after eliminating noise around the region of interest is segmenting the image using Chan-Vese algorithm [37] to eliminate the false bright structures around the tumour. Chan-Vese algorithm is an active contour algorithm that uses an initial contour within the image. The algorithm then expands this contour iteratively using an evolution equation until it surrounds the foreground region. The level-set functions used as evolution equation in this algorithm are $\varphi[i, j, t]$, where i and j represent - pixels coordinates and t is time. Chan-Vese segmentation algorithm operates by minimizing the fitting energy function described by the following - equation:

$$\varphi_t = \partial(\varphi)\left[\mu p\left(\int \partial(\varphi)|\nabla_\varphi|\right)^{p-1} div\left(\frac{\nabla_\varphi}{|\nabla_\varphi|}\right) - v - \lambda_1(I - c1)^2 p + \lambda_2(I - c2)^2\right], \tag{2}$$

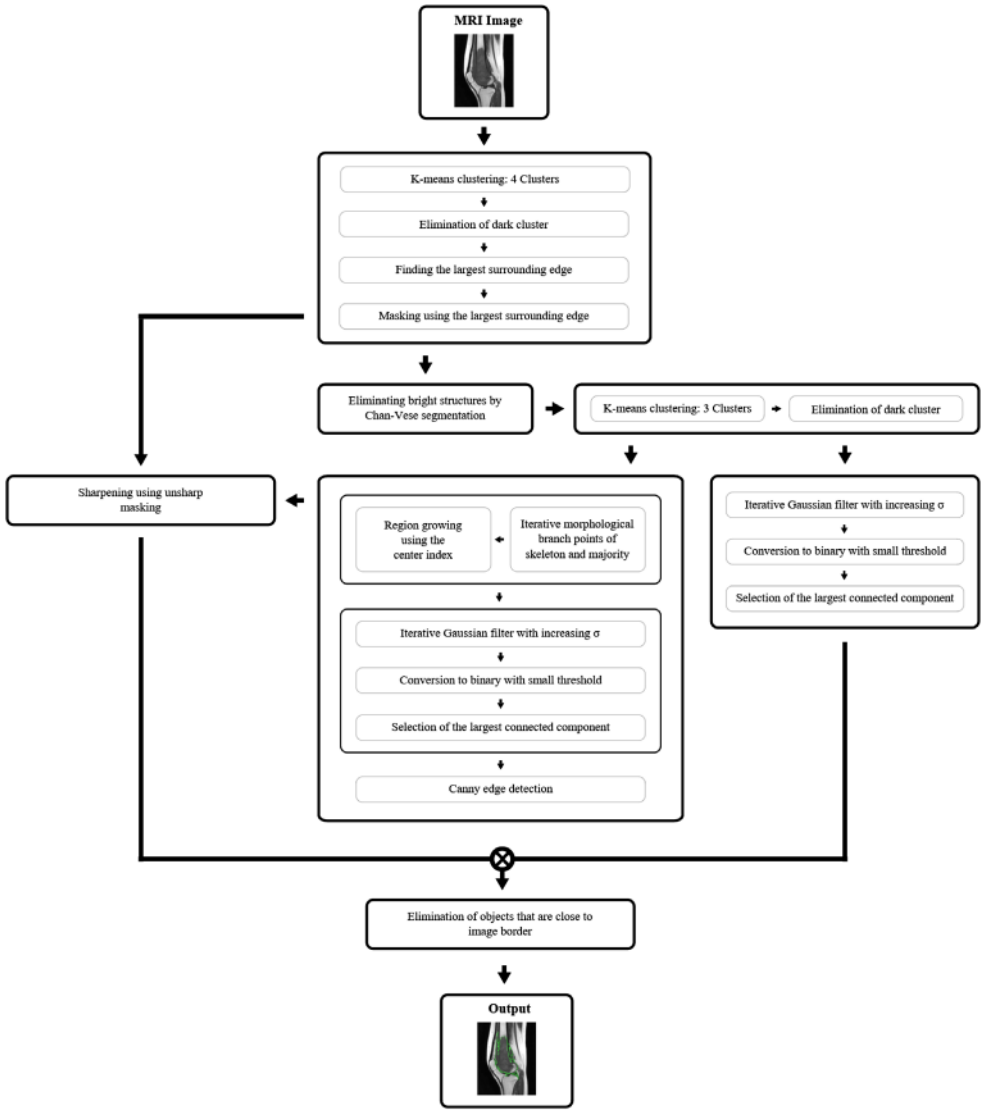

FIGURE 1 Block diagram of the proposed technique

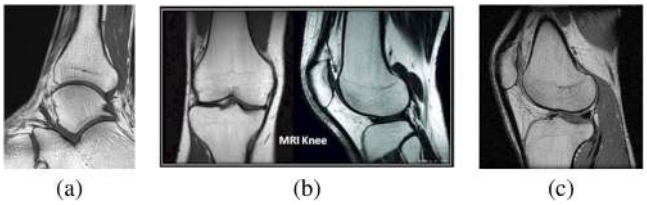

FIGURE 2 Examples of normal bone MRI images

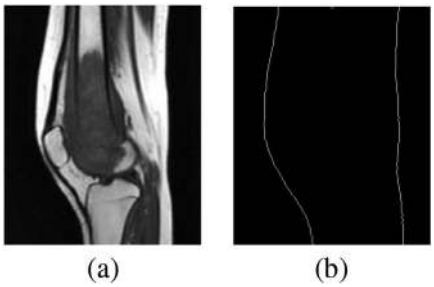

FIGURE 3 Finding the largest surrounding edge in the MRI image. (a) Original image (b) the largest surrounding edge

where p, μ, v, λ_1 and λ_2 are parameters specified by the user, c1 and c2 are the average values of the image.

The discrete form representation of the differential equation (2) at pixel (i, j) is:

$$\varphi_{i,j}^{n+1} = F_1\varphi_{i+1,j}^{n+1} + F_2\varphi_{i-1,j}^{n+1} + F_3\varphi_{i,j+1}^{n+1} + F_4\varphi_{i,j-1}^{n+1} + Fp_{i,j}, \tag{3}$$

where

$$F_i = \frac{\nabla t\partial_h(\varphi_{i,j}^n)\mu(pL(\varphi^n)^{p-1}C_i}{h + \nabla t\partial_h(\varphi_{i,j}^n)\mu(pL(\varphi^n)^{p-1}(C1 + C2 + C3 + C4)}, \quad i = 1, 2, 3, 4 \tag{4}$$

$$F = \frac{h}{h + \nabla t \partial_h(\varphi^n_{i,j})\mu(pL(\varphi^n)^{p-1}(C1 + C2 + C3 + C4)}, \quad (5)$$

$$p_{i,j} = \varphi^n_{i,j} - \nabla t \partial_h(\varphi^n_{i,j})[v + \lambda_1(I_{i,j} - c1(\varphi^n))^2 - \lambda_2(I_{i,j} - c2(\varphi^n))^2], \quad (6)$$

where $h = 1$ represents the implied pixel spacing, n and L are the number of iterations and the the perimeter length of the zero level set for φ and ∂_h, and $C1, C2, C3, C4$ are predefined constants.

K-means clustering is applied again after eliminating the high-intensity cluster using Chan-Vese segmentation. The image is subsequently divided into three clusters by the second implementation of the K-means clustering and the dark-cluster is eliminated. The resultant image goes into two parallel further processing:

The first process is iterative Gaussian filtering using the filter described by the following equation:

$$G(x,y) = \frac{1}{2\pi(\sigma_k)^2} e^{\frac{-(x^2+y^2)}{2(\sigma_k)^2}}, k = 1, 2, 3, \ldots \quad (7)$$

This iterative filtering is performed while converting pixels to binary using a small threshold value (0.1) and selecting the largest connected component (object). The iterative process produces multiple objects and at the end, the object that has the lowest number of pixels is selected.

The second process consists of three steps: the first step comprises iterative morphological operation [38–41], thinning (removing pixels so that the object shrinks to a minimally connected stroke), finding branch points of the skeleton (setting pixels to zeros except for the one in the center of a 5x5 patch if the third row and third column were ones), majority pixel conversion (setting a pixel to 1 if most of the neighborhood pixels are ones), and selecting the largest connected component. These operations are repeated until the number of objects equal to one followed by region growing [42]. The second and third steps are iterative Gaussian filtering and masking using Canny edge detection. Finally, the tumour region is obtained from the intersection of these two parallel processes with the sharpened version of the original image. The segmented tumour is considered to be true if it does not touch the boundaries (borders) of the image while similar objects that fall on the boundaries are eliminated since they usually represent non-tumourous tissues.

Figure 4 shows the application of the K-means clustering and Chan-Vese algorithm on an MRI image. K-means clustering eliminates the dark regions as shown in Figure 4(a) and Figure 4(c) while Chan-Vese algorithm eliminates the bright regions as shown in Fig 4(b). Figure 5 shows the outcomes of applying iterative Gaussian filtering, iterative morphological branch points of skeleton and majority, and region growing (adding neighbouring pixels that are similar in terms of intensity in order to increase the size of the area). The iterative Gaussian filtering eliminates false surrounding edges as shown in Figure 5(a). Iterative branch points of skeleton and majority operations enhance the region of interest as shown in Figure 5(b). Region growing is used to expand the region of interest as shown in Figure 5(c).

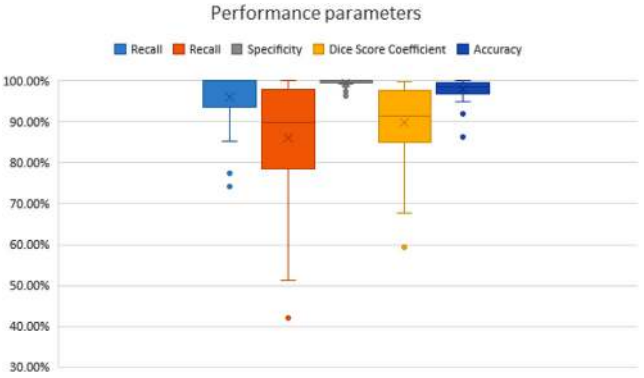

FIGURE 4 Box plot of the performance parameters calculated by the proposed technique

A pseudocode algorithm for the proposed technique is given in Algorithm 1.

4 | RESULTS AND DISCUSSION

The proposed technique was tested on a PC with Intel Core i5-7300U 2.7 GHz processor and 8GB of RAM and the code was written using Matlab R2015a. Fifty MRI images that include T1-weighted, T2-weighted, and PD in coronal and sagittal view planes were used in the testing [43–54]. The technique was able to accurately segment the tumours in all of the cases regardless of the variations in intensity values, size, and position of each tumour with respect to other surrounding non-tumourous regions as shown in Figures 4– 16.

In order to evaluate and validate the segmentation results, performance parameters: precision, recall, specificity, Dice score coefficient (DSC), similarity index (SI), and accuracy were calculated using the obtained values for the true positive (TP), the true negative (TN), false positive (FP), and false negative (FN) pixels. Where TP is the number of pixels which are assigned a value of one for matching the ground truth, FP is the number of pixels which are assigned a value of one despite not matching the ground truth, FN is the number of pixels which are assigned a value of zero in case of not matching the ground truth, and TN is the number of pixels which are assigned a value of zero despite matching the ground truth. The performance parameters were calculated using the following equations.

$$\text{Precision} = \frac{TP}{(TP + FP)} \times 100\%, \quad (8)$$

$$\text{Recall} = \frac{TP}{(TP + FN)} \times 100\%, \quad (9)$$

$$\text{Specificity} = \frac{TN}{(TN + FP)} \times 100\%, \quad (10)$$

FIGURE 5 Osteosarcoma segmentation in images 1–4

FIGURE 6 Osteosarcoma segmentation in images 5–8

FIGURE 7 Osteosarcoma segmentation in images 9–12

FIGURE 8 Osteosarcoma segmentation in images 13–16

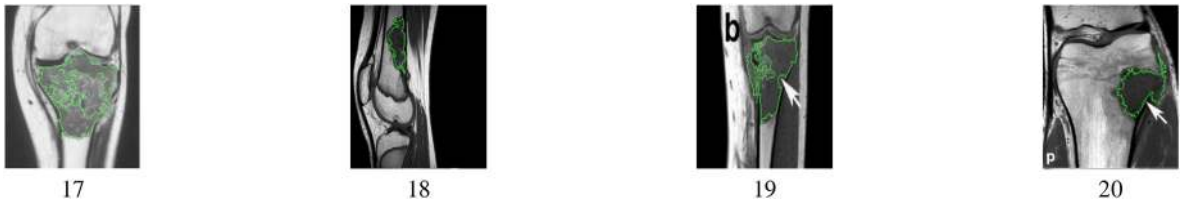

FIGURE 9 Osteosarcoma segmentation in images 17–20

FIGURE 10 Osteosarcoma segmentation in images 21–24

FIGURE 11 Osteosarcoma segmentation in images 25–28

FIGURE 12 Osteosarcoma segmentation in images 29–32

FIGURE 13 Osteosarcoma segmentation in images 33–36

FIGURE 14 Osteosarcoma segmentation in images 37–40

FIGURE 15 Osteosarcoma segmentation in images 41–44

FIGURE 16 Osteosarcoma segmentation in images 45–48

Algorithm 1 Proposed technique algorithm

```
//Eliminating dark and false surrounding regions:
Clusters = 4
MRIimage ←K-means(MRIimage,Clusters)
MRIimage ←MRIimage - MRIimage(DarkCluster)
MRIimage ←MRIimage * Filledimage(L.Edge(MRIimage))
//Eliminating bright and dark regions:
Clusters = 3
MRIimage ←MRIimage - ChanVese(MRIimage,BrightCluster)
MRIimage ←K-means(MRIimage,Clusters)
MRIimage ←MRIimage - MRIimage(DarkCluster)
//Iterative Gaussian Filtering:
while Sigma ≤ 28 do
   Sigma = 2
   MRIimage1 ←GaussianFiltering(MRIimage,Sigma)
   MRIimage1 ←BinaryConversion(MRIimage,0.1)
   MRIimage1 ←MRIimage(LargestComponent)
   Sigma ←Sigma+1
end while
/Morphological operations and filtering:
while Objects ≤ 1 do
   Value = 5
   MRIimage2 ←MorphologicalThinning(MRIimage,Value)
   MRIimage2 ←MorphologicalBranchPoints(MRIimage2,1)
   MRIimage2 ←MorphologicalMajority(MRIimage2,1)
   MRIimage2 ←MRIimage2(LargestComponent)
   Value ←Value+1
end while
/Canny edge:
MRIimage3 ←CannyEdge(MRIimage)
MRIimage3 ←Inverse(MRIimage3)
/Sharpening:
Radius = 10
Amount = 7
MRIimage4 ←Sharpen(MRIimage,Radius,Amount)
/Combining the images:
MRIimage5 ←MRIimage*MRIimage4 ∗MRIimage3
MRIimage5 ←MRIimage5*MRIimage2 ∗MRIimage1
/Eliminating border objects:
while Objects ≥ 1 do
   PossibleBorderobjects ←EuclideanDistance(MRIimage5,Borders)
   if EuclideanDistance(MRIimage5, Borders) < 2 then
      Borderobjects ←Borderobjects+PossibleBorderobjects
   end if
end while
MRIimage5 ←MRIimage5-Borderobjects
```

FIGURE 17 Osteosarcoma segmentation in images 49 and 50

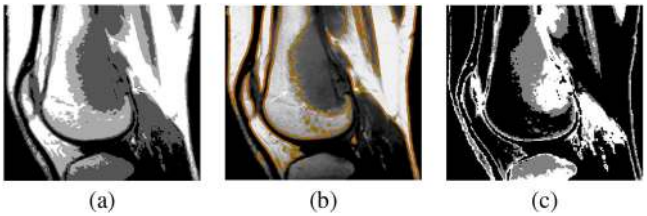

FIGURE 18 K-means clustering and Chan-Vese algorithms (a) using four clusters to eliminate dark cluster (b) Chan-Vese algorithm to detect bright regions (c) using three clusters after eliminating bright regions

$$\text{DSC} = \frac{2 \times TP}{(2 \times TP + FP + FN)} \times 100\%, \tag{11}$$

$$\text{Accuracy} = \frac{TP + TN}{(TP + FP + FN + TN)} \times 100\%, \tag{12}$$

The overall average running time for the MRI images is 3.19 minutes which is lower than the average running time using deep leaning segmentation [20]. A box plot showing the dispersion of the performance parameters is given in Figure 19. The quartile ranges of the scores are displayed for every performance parameter with whiskers and dots '.' representing outliers while crosses 'x' represent the average score. The average values of precision, recall, specificity, Dice score coefficient, and accuracy are 95.96%, 86.15%, 99.51%, 89.84%, and 98.02%, respectively. It can be noticed that the proposed technique achieved quite high values for precision, specificity, and accuracy as all of their average values are greater than 95% while the average values for recall and Dice score coefficient are relatively lower. It is worth noting that the average accuracy (98.02%) is higher than the values reported by Rajeswari et al., 2010 [25], Huang et al., 2016 [28], and and Li et al., 2010 [27] as shown in Table 1.

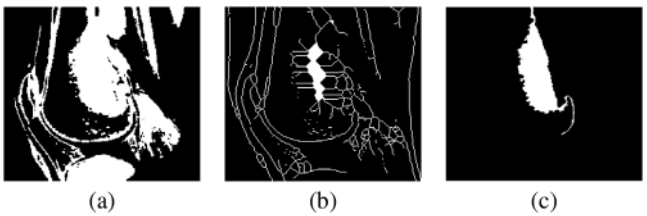

FIGURE 19 Performing iterative Gaussian filtering and morphological operations besides region growing (a) iterative Gaussian filtering (b) iterative branch points and majority (c) region growing

TABLE 1 Comparison between the performance of the proposed technique and other MRI osteosarcoma segmentation techniques

Technique	Precision	Recall	Specificity	DSC	Accuracy	Time (seconds)
Multi-Target [28]	-	-	-	-	83.5%	-
Dynamic Harmony [26]	-	79.9%	-	80%	-	-
Logistic Regression (LR) [55]	72.56%	74.38%	-	70.21%	-	Instantaneous
LSVM [55]	73.57%	73.57%	-	71.43%	-	Instantaneous
DNN [55]	76.57%	86.12%	-	73.02%	-	Instantaneous
Proposed technique	95.96%	86.15%	99.51%	89.84%	98.02%	191.4

5 | CONCLUSION

A technique to segment Osteosarcoma tumours in MRI images have been developed and tested. The technique used a combination of K-means clustering, Chan-Vese segmentation, iterative Gaussian filtering, Canny edge detection, and region growing in order to segment the tumour and distinguish between the tumour and other non tumourous surrounding tissues such as bones. The technique was tested on different types of MRI images which included T1 and T2 with coronal plane and sagittal plane. The technique was able to segment the osteosarcoma tumours in MRI images successfully with an overall accuracy of 98.02% which is higher than the accuracy reported using other segmentation methods. The future extension of this work will focus on 3D segmentation of osteosarcoma in MRI and CT images.

ORCID

Mohamed Nasor https://orcid.org/0000-0002-4833-4363
Walid Obaid https://orcid.org/0000-0002-3604-0907

REFERENCES

1. Meyers, P.A., et al.: Osteosarcoma: The addition of muramyl tripeptide to chemotherapy improves overall survival-a report from the children's oncology group. J. Clin. Oncol. 26(4), 633–638 (2008)
2. Picci, P.: Osteosarcoma (osteogenic sarcoma). Orphanet J. Rare Dis. 2(1), 6 (2007)
3. GJ, C., et al.: Prediction model of chemotherapy response in osteosarcoma by 18f-fdg PET and MRI. J. Nucl. Med. 50(9), 1435–1440 (2009)
4. Ritter, J., Bielack, S.: Osteosarcoma. Ann. Oncol. 21, vii320–vii325 (2010)
5. Fletcher, C.D., et al.: Pathology and Genetics of Tumours of Soft Tissue and Bone, 4, 264–271. IARC Press, Lyon (2002)
6. Zhang, C., et al.: Brain tumor segmentation based on hybrid clustering and morphological operations. Int. J. Biomed. Imaging, 1–11 (2019)
7. Karuna, Y., et al.: Brain tissue classification using PCA with hybrid clustering algorithms. Int. J. Eng. Technol. 7(2), 536–540 (2018)
8. Hu, H., et al.,: Hybrid segmentation of left ventricle in cardiac MRI using Gaussian-mixture model and region restricted dynamic programming. Magn. Reson. Imaging 31, 575–584 (2013)
9. Alsmadi, M.: MRI brain segmentation using a hybrid artificial bee colony algorithm with fuzzy-c mean algorithm. J. Appl. Sci. 15(1), 100–109 (2015)
10. Frangi, A.F., et al.: Bone tumor segmentation from MR perfusion images with neural networks using multi-scale pharmacokinetic features. Image Vis. Comput. 19(9–10), 679–690 (2001)
11. Glass, J.O., Reddick, W.E.: Hybrid artificial neural network segmentation and classification of dynamic contrast-enhanced MR imaging (DEMRI) of osteosarcoma. Magn. Reson. Imaging 16(9), 1075–1083 (1998)
12. CHEN, C.X., et al.: Osteosarcoma segmentation in MRI based on Zernike moment and SVM. Chinese J. Biomed. Eng. 22(2), 70–78 (2013)
13. Tripathy, R., et al.,: Gaussian processes with built-in dimensionality reduction: Applications to high-dimensional uncertainty propagation. J. Comput. Phys. 321, 191–223 (2016)
14. Zhang, X., et al.,: Feature selection in mixed data: A method using a novel fuzzy rough set-based information entropy. Pattern Recognit. 56, 1–15 (2016)
15. Girshick, R., et al.: Region-based convolutional networks for accurate object detection and segmentation. IEEE Trans. Pattern Anal. Mach. Intell. 38(1), 142–158 (2015)
16. Kraus, O.Z., et al.: Classifying and segmenting microscopy images with deep multiple instance learning. Bioinformatics 32(12), i52–i59 (2016)
17. Moeskops, P., et al.: Automatic segmentation of MR brain images with a convolutional neural network. IEEE Trans. Med. Imaging 35(5), 1252–1261 (2016)
18. Zhang, W., et al.,: Deep convolutional neural networks for multi-modality isointense infant brain image segmentation. NeuroImage 108, 214–224 (2015)
19. Ertas, G., et al.: Computerized detection of breast lesions in multi-centre and multi-instrument DCE-MR data using 3D principal component maps and template matching. Phys. Med. Biol. 56(24), 7795–7811 (2011)
20. Pereira, S., et al.: Brain tumor segmentation using convolutional neural networks in MRI images. IEEE Trans. Med. Imaging 35(5), 1240–1251 (2016)
21. Long, J., et al.: Fully convolutional networks for semantic segmentation. In: Proceedings of the IEEE Conference on Computer Vision and Pattern Recognition, pp. 3431–3440. IEEE, Piscataway (2015)
22. Chen, C., et al.: Osteosarcoma segmentation in CT images based on hybrid relative fuzzy connectedness. In: 5th International Conference on BioMedical Engineering and Informatics, pp. 324–328. IEEE, Piscataway (2012)
23. Ma, J., et al.: Segmentation of multimodality osteosarcoma MRI with vectorial fuzzy-connectedness theory. In: International Conference on Fuzzy Systems and Knowledge Discovery, pp. 1027–1030. IEEE, Piscataway (2005)
24. Hong, F., et al.: Segmentation of osteosarcoma based on analysis of blood-perfusion EPI series. In: International Conference on Communications, Circuits and Systems (IEEE Cat No 04EX914), vol. 2, pp. 955–959. IEEE, Piscataway (2004)
25. Rajeswari, M., et al.: Spatial multiple criteria fuzzy clustering for image segmentation. In: Second International Conference on Computational Intelligence, Modelling and Simulation, pp. 305–310. IEEE Computer Society, Los Alamitos (2010)
26. Mandava, R., et al.: Osteosarcoma segmentation in MRI using dynamic harmony search based clustering. In: International Conference of Soft Computing and Pattern Recognition, pp. 423–429. IEEE, Piscataway (2010)
27. Li, C., Liu, Y.: Research on automatic recognition of lesion areas of osteosarcoma X-ray images based on support vector machine. J. Med. Inform. 31(9), 32–34 (2010)
28. Huang, W.B., et al.: Multi-target osteosarcoma MRI recognition with texture context features based on CRF. In: International Joint Conference on Neural Networks (IJCNN), pp. 3978–3983. IEEE, Piscataway (2016)
29. Zhang, R., et al.,: Multiple supervised residual network for osteosarcoma segmentation in CT images. Comput. Med. Imaging Graphics 63, 1–8 (2018)

30. Kapur, T., et al.: Model-based segmentation of clinical knee MRI. In: International Workshop on Model-Based 3D Image Analysis, pp. 97–106. IEEE, Piscataway (1998)
31. Ankle MRI examination. https://radiologyassistant.nl/musculoskeletal/ankle-mri-examination. Accessed May 2020
32. MRI knee. https://www.swslhd.health.nsw.gov.au/medicalImaging/serv_MRI_Knee.html. Accessed May 2020
33. Wu, M.N., et al.: Brain tumor detection using color-based K-means clustering segmentation. In: Third International Conference on Intelligent Information Hiding and Multimedia Signal Processing (IIH-MSP 2007), vol. 2, pp. 245–250. IEEE, Piscataway (2007)
34. van den Boomgaard, R., van Balen, R.: Methods for fast morphological image transforms using bitmapped binary images. CVGIP: Graph. Models Image Process. 54(3), 252–258 (1992)
35. Adams, R.: Radial decomposition of disks and spheres. CVGIP: Graph. Models Image Process. 55(5), 325–332 (1993)
36. Jones, R., Soille, P.: Periodic lines: Definition, cascades, and application to granulometries. Pattern Recognit. Lett. 17(10), 1057–1063 (1996)
37. Getreuer, P.: Chan-Vese segmentation. Image Process. On Line 2, 214–224 (2012)
38. Haralick, R.M., Shapiro, L.G.: Computer and Robot Vision, vol. 1, 28–48. Addison-Wesley, Reading (1992)
39. Kong, T.Y., Rosenfeld, A.: Topological Algorithms for Digital Image Processing, vol. 19, 31–98. Elsevier, New York (1996)
40. Lam, L., et al.: Thinning methodologies: A comprehensive survey. IEEE Trans. Pattern Anal. Mach. Intell. 14(9), 869–885 (1992)
41. Pratt, W.K.: Digital Image Processing, 307–344. Wiley-Interscience, Hoboken (1991)
42. Zhang, Z., et al.: Border detection on digitized skin tumor images. IEEE Trans. Med. Imaging 19(11), 1128–1143 (2000)
43. Osteosarcoma of femur radiograph. http://manju-imagingxpert.blogspot.com/2011/10/osteosarcoma-of-femur-radiograph-and.html?m=1. Accessed May 2020
44. FDG-PET/CT complements bone scan with respect to the detection of skip metastasis of osteosarcoma: A case report. https://synapse.koreamed.org. Accessed May 2020
45. Osteosarcoma tibia. https://radiopaedia.org/cases/osteosarcoma-tibia. Accessed May 2020
46. Osteosarcoma 6. https://basicmedicalkey.com/osteosarcoma-6/. Accessed May 2020
47. Giant cell tumor of bone benign but still worthy of vigilance. https://consultqd.clevelandclinic.org/giant-cell-tumor-of-bone-benign-but-still-worthy-of-vigilance/amp/. Accessed May 2020
48. Giant cell tumor of bone. https://www.wikidoc.org/index.php/Giant_cell_tumor_of_bone. Accessed May 2020
49. Bone cancer, MRI scan. https://www.sciencephoto.com/media/253741/view. Accessed May 2020
50. Two mutations to ewing sarcoma. medicalxpress.com. Accessed May 2020
51. Spindle cell sarcoma. https://www.diagnosticimaging.com/case-studies/spindle-cell-sarcoma. Accessed May 2020
52. Malignant bone tumors II: Miscellaneous tumors. https://radiologykey.com/malignant-bone-tumors-ii-miscellaneous-tumors/. Accessed May 2020
53. Slavchev, S.A., et al.: An active giant cell tumor of the patella: A case report. Cureus 9(9), e1642 (2017)
54. Henninger, B., et al.: Ewing sarcoma versus osteomyelitis: Differential diagnosis with magnetic resonance imaging. Skeletal Radiol. 42, 1097–1104 (2013)
55. Kayal, E.B., et al.: Segmentation of osteosarcoma tumor using diffusion weighted MRI: a comparative study using nine segmentation algorithms. Signal, Image Video Process. 14, 727–735 (2019)

How to cite this article: Nasor M, Obaid W. Segmentation of osteosarcoma in MRI images by K-means clustering, Chan-Vese segmentation, and iterative Gaussian filtering. *IET Image Process.* 2021;15:1310–1318.
https://doi.org/10.1049/ipr2.12106